

Supplementary Information

Band Gap Engineering of Ce-Doped Anatase TiO₂ through Solid Solubility Mechanisms and New Defect Equilibria Formalism

1. INTRODUCTION

Table I provides a comprehensive summary of the reported studies of Ce doping of TiO₂ by experimentation and density functional theory (DFT).

Table I. Comprehensive survey of characteristics of Ce-doped TiO₂ (all uncompensated stoichiometry)

Method of Fabrication	TiO ₂ Form	Polymorph	Ce Dopant Level (mol%)	Lattice Parameters (nm)				Implied Solubility Limit	Crystallite Size (nm)		Optical Indirect Band Gap (eV)		Comments	Ref
				Undoped		Doped			Undoped	Doped	Undoped	Doped		
				<i>a, b</i>	<i>c</i>	<i>a, b</i>	<i>c</i>							
Sol-gel spin coating on unknown substrate 500°C, 3 h	Film	Anatase	1.00	-	-	-	-	-	8.00	32.0	3.45	3.07	Decreased defect concentrations, <i>e.g.</i> , [V _O ^{••}], as shown by decreasing PL peak intensities	1
Sol-gel 500°C, 2 h	Powder	Anatase	1.00	0.3795	0.9499	0.3790	0.9495	-	10.3	17.7	3.14	3.05	Increased [V _O ^{••}] and decreased porosity, surface area, and lattice microstrain	2
Evaporation-induced self-assembly 400°, 500°, 600°C, 2 h	Powder	Anatase	0.05	0.3800 (400°C)	0.9511 (400°C)	0.4428 (400°C)	0.9515 (400°C)	-	9.30 (400°C)	6.20 (400°C)	-	2.10 (400°C)	Enhanced photocatalytic performance in sample annealed at 500°C	3
									11.8 (500°C)	7.90 (500°C)	3.10 (500°C)	1.85 (500°C)		
									15.0 (600°C)	12.3 (600°C)	-	1.78 (600°C)		
Sol-gel 600°C, 2 h	Powder	Anatase	Unknown	0.3783	0.9452	0.3795	0.9656	-	44.8	11.1	3.19	2.48	-	4
TiO ₂ Hydrothermal 400°C, 1h Ce-TiO ₂ Impregnation method 300°, 350°, 400°, 450°, 500°C, 1 h	Nano-tubes	TiO ₂ Anatase + Rutile at 400°C Ce-TiO ₂ Anatase at 300°-500°C	0.10 0.15 0.20 0.30 0.40 0.50	-	-	-	-	0.15 mol% Ce-TiO ₂ (400°C)	-	-	-	Red shifted	-	5
TiO ₂ nanoparticle by Hydrothermal 220°C, 12h TiO ₂ paste on screen print 500°C, 15 min	Film	Anatase	0.10 0.30 0.60 0.90	0.3789	0.9498	0.3791 (0.10%)	0.9527 (0.10%)	0.10 mol% Ce-TiO ₂	13.07	12.30 (0.10%)	3.23	3.15 (0.10%)	Lattice expansion in <i>c</i> direction due to Ce interstitial solubility; reverse trend at higher Ce levels owing to Ce surface segregation	6
						0.3787 (0.30%)	0.9532 (0.30%)			12.16 (0.30%)				
						0.3787 (0.60%)	0.9509 (0.60%)			12.68 (0.60%)				

Method of Fabrication	TiO ₂ Form	Polymorph	Ce Dopant Level (mol%)	Lattice Parameters (nm)				Implied Solubility Limit	Crystallite Size (nm)		Optical Indirect Band Gap (eV)		Comments	Ref
				Undoped		Doped			Undoped	Doped	Undoped	Doped		
				a, b	c	a, b	c							
						0.3786 (0.90%)	0.9513 (0.90%)		12.25 (0.90%)					
Sol-gel 70°, 400°, 500°, 600°, 700°, 800°C, 6 h	Powder	Ce-TiO ₂ Anatase at 70°, 400°C and Anatase + Rutile at 500°-800°C	0.002 0.003 0.004 0.008 0.012 0.024	-	-	-	-	0.004 mol% Ce-TiO ₂ (600°C)	-	4.00- 6.00	3.20 (500°C)	2.50 (0.002% 500°C) 2.50 (0.003% 500°C) 2.48 (0.004% 500°C) 2.49 (0.008% 500°C) 2.40 (0.012% 500°C) 2.35 (0.024% 500°C)	Increasing rutile/anatase ratio and increasing E _g with increasing Ce concentration	7
Sol-gel + carbon spheres as template 500°C, 3 h	Hollow spheres	Anatase	1.00 2.00 4.00 6.00	-	-	-	-	4.00 mol% Ce-TiO ₂	-	10.9 (1.00%) 10.2 (2.00%) 9.20 (4.00%) 8.30 (6.00%)	-	Red shifted	-	8
Sol-gel dip-coating on stainless steel TiO ₂ : 450°C, 3 h TiO ₂ -Ce: 550°C, 3 h	Film	Anatase	0.01	0.3774	0.9443	0.3797	0.9533	-	16.1	9.10	-	Red shifted	Greater defect density and lattice distortion on grain boundaries due to lattice expansion	9
Sputtering on glass or ITO substrate	Film	TiO ₂ Anatase + rutile	0.40	-	-	-	-	-	28.0 (glass)	23.0 (glass)	3.13 (glass)	3.20 (glass)	Crystallographic effect of substrate on Ce-TiO ₂ : Glass: anatase	10

Method of Fabrication	TiO ₂ Form	Polymorph	Ce Dopant Level (mol%)	Lattice Parameters (nm)				Implied Solubility Limit	Crystallite Size (nm)		Optical Indirect Band Gap (eV)		Comments	Ref		
				Undoped		Doped			Undoped	Doped	Undoped	Doped				
				<i>a, b</i>	<i>c</i>	<i>a, b</i>	<i>c</i>									
temperature, 250°C		(glass, ITO)						22.0 (ITO)	20.0 (ITO)	3.27 (ITO)	3.21 (ITO)	ITO: anatase + rutile				
Supramolecular-templated sol-gel spin coating on single-crystal Si(111) wafers 350°C, 4 h	Film	Anatase	0.20	-	-	-	-	0.30 mol% Ce-TiO ₂	8.50	8.00 (0.20%)	-	-	Reduction in density of surface-active sites, resulting in reduced photocatalytic activity	11		
			0.30							7.50 (0.30%)						
			0.75							6.80 (0.75%)						
			2.00							6.60 (2.00%)						
			5.00							4.50 (5.00%)						
			10.0													
30.0																
Sol-gel 400°C, 5 h	Powder	Anatase	0.08	-	-	-	-	0.40 mol% Ce-TiO ₂	26.35	10.38 (0.08%)	-	-	-	12		
			0.40							14.26 (0.40%)						
			1.00							24.51 (1.00%)						
			1.50							21.45 (1.50%)						
			2.50							20.06 (2.50%)						
Sol-gel spin coating on glass 450°C, 2 h	Film	Anatase	0.10 0.25 0.50 1.00	-	-	-	-	0.25 mol% Ce-TiO ₂	-	-	3.48 3.46 3.45 3.44	Optimal photocatalytic performance at 0.25 mol% Ce	13			
Sol-gel auto-igniting synthesis 550°, 600°, 650°, 700°, 750°, 800°, 850°, 900°C, 2 h	Powder	Anatase at 550°C	1.25	0.377	0.972			2.50 mol% Ce-TiO ₂ (800°C)	28.0	23.0 (1.25%)	-	Red shifted	Phase transition from anatase to rutile at high temperatures; greatly reduced solubility in rutile relative to that in anatase	14		
			2.50							0.379 (2.50%)					0.975 (2.50%)	15.0 (2.50%)
			5.00							0.380 (5.00%)					0.979 (5.00%)	11.0 (5.00%)
Sol-gel 600°C, 6 h	Powder	Anatase + rutile	0.25 0.50 1.00	-	-	-	-	0.50 ≤ mol% Ce-TiO ₂	-	-	3.20	(1) Increasing photocatalytic activity with increasing [Ce] ≤ 1	15			

Method of Fabrication	TiO ₂ Form	Polymorph	Ce Dopant Level (mol%)	Lattice Parameters (nm)				Implied Solubility Limit	Crystallite Size (nm)		Optical Indirect Band Gap (eV)		Comments	Ref
				Undoped		Doped			Undoped	Doped	Undoped	Doped		
				<i>a, b</i>	<i>c</i>	<i>a, b</i>	<i>c</i>							
			2.00 3.00 5.00 9.00									mol% (2) Reverse trend for 1.00 mol% > [Ce] ≤ 2.00 mol% (3) Electron-hole recombination rate reduction from charge transfer to surrounding medium facilitated by oxidised Ce ⁴⁺ and reduced Ce ³⁺ on the surface (4) Surface-scattering of light by precipitated CeO ₂ at [Ce] ≥ 2.00 mol%		
DFT simulation	TiO ₂ (001) surface	Anatase	2.60	-	-	0.381 (DFT)	0.973 (DFT)	-	-	-	2.69 Bulk (DFT)	2.71 Bulk (DFT)	Expansion of [CeO _x] polyhedra upon substitution, where outermost M-O bond lengths at surface longer than those in bulk	16
						0.378 (Experimental)	0.951 (Experimental)				2.14 TiO ₂ (001) surface (DFT)	-		
											3.23 Bulk (Experimental)	2.98 Bulk (Experimental)		

2. EXPERIMENTAL PROCEDURE

2.1 Materials

Titanium (IV) tetra-isopropoxide (TTIP; $\text{Ti}(\text{OCH}(\text{CH}_3)_2)_4$, 97.00 wt%) was used as precursor for TiO_2 , cerium (III) nitrate hexahydrate ($\text{Ce}(\text{NO}_3)_3 \cdot 6\text{H}_2\text{O}$, 99.99 wt%) was used as dopant, and isopropanol ($\text{C}_3\text{H}_8\text{O}$, 99.99 wt%) was used as solvent. An aqueous solution (in deionised water) of standard dye ¹⁷⁻¹⁹ (methylene blue, $\text{C}_{16}\text{H}_{18}\text{N}_3\text{SCl}$, M9140, dye content ≥ 82 wt%) was used for photocatalytic performance testing. All the chemicals were purchased from Sigma-Aldrich.

2.2 Substrates

The substrates consisted of unpolished fused silica (SiO_2) of dimensions 20 mm x 20 mm x 1 mm, obtained from Pilkington, United Kingdom.

2.3 Procedures

Prior to deposition, the substrates were ultrasonically cleaned for 5 min in an aqueous detergent solution, followed by sequential rinsing with distilled water, ethanol, and acetone. The substrates then were dried on a hot plate at 120°C for 5 min, after which they were used immediately for deposition.

The main TiO_2 solution was prepared by dissolving 0.1 M titanium tetra-isopropoxide, TTIP, in 100 mL of isopropanol by magnetically stirring at 60°C for 15 min. The doping solution was prepared by dissolving 0.01 M solution of $\text{Ce}(\text{NO}_3)_2 \cdot 6\text{H}_2\text{O}$ in 100 mL of isopropanol by magnetically stirring at room temperature for 15 min. These solutions were combined in appropriate ratios and homogenised by magnetic stirring at 60°C for 15 min to obtain 0.01-0.09 mol% Ce (low Ce) and 0.10-0.90 mol% (high Ce) (metal basis).

Thin films were prepared by spin coating (Laurell WS-650SZ-6NPP/LITE) under vacuum (mechanical vacuum pump, ~100 Pa) by dropping ten drops on an unpolished fused SiO_2 substrates in all cases (except for amplitude-modulated Kelvin probe force microscopy, which used Si (110) substrates) spun at 2000 rpm over 15 s, followed by rotational drying for an additional 5 s. The sample was removed from the spin coater and dried on a hotplate at 65°C for 10 min. These processes were repeated six more times to obtain seven deposition layers (seventy drops). Each set of samples was annealed in air in a muffle furnace at 450°C

for 2 h (heating rates $0.5^{\circ}\text{C}\cdot\text{min}^{-1}$ over 20° - 200°C and $1^{\circ}\text{C}\cdot\text{min}^{-1}$ over 200° - 450°C), followed by natural cooling.

2.4 Characterisation

2.4.1 DFT

First-Principles Calculations

Spin-polarised first-principles calculations based on density functional theory (DFT) were used to estimate the electronic energy levels associated with substitutional and interstitial Ce defects in bulk anatase. The PBEsol functional²⁰ as implemented in the VASP software package²¹ was employed. A “Hubbard- U ” scheme²² with a standard^{16, 23} $U = 4$ eV was applied for superior treatment of the localised Ce $4f$ and Ti $3d$ electronic orbitals (it was confirmed that the adopted PBEsol+ U setup reproduced closely the experimental lattice parameters of anatase of $a_0 = b_0 = 0.378$ nm and $c_0 = 0.957$ nm). The “projector augmented wave” method was used to represent the ionic cores²⁴ by considering the following electrons as valence: Ce $4f$, $5d$, and $6s$; Ti $3d$, $4s$, and $3p$; O $2s$ and $2p$. Wave functions were represented in a plane-wave basis truncated at 650 eV. For integrations within the Brillouin zone, a Monkhorst-Pack k-point grid²⁵ with density equivalent to $16 \times 16 \times 16$ for the anatase unit cell was used. Geometry relaxations were performed using a conjugate-gradient algorithm that allows cell volume and cell shape variations; the geometry relaxations were halted once all of the forces on the atoms fell below 0.1 eV \cdot nm $^{-1}$. Using these technical parameters, zero-temperature energies that converged to within 0.5 meV per formula unit were obtained. The singlet and triplet spin configurations were analysed systematically for each iteration in order to determine reliable ground-state energies. The hybrid HSE06 exchange-correlation functional²⁶ was used and the equilibrium geometries generated by the PBEsol+ U setup were adopted in order to estimate the electronic energy levels in reasonable computation times. The range-separated hybrid HSE06 exchange-correlation functional²⁶ (with a Hartree-Fock mixing parameter of 0.25 and screening parameter of 0.20) was used. A periodic supercell consisting of a $3 \times 3 \times 1$ repetition of the conventional anatase unit cell containing 12 ions was used to describe stoichiometric and Ce-doped bulk TiO_2 . The defect configurations were generated using one substitutional or interstitial Ce ion in the 108-ion supercell. The reduced species Ti^{3+} and Ce^{3+} were generated either by introducing an oxygen vacancy in the supercell or by constraining the total number of electrons in the system. The value of the theoretical valence and conduction energy band edges referred to the Fermi

energy level were determined through analysis of the projected densities of electronic states obtained²³ in the spin-polarised DFT calculations.

2.4.2 Materials

Mineralogy and Crystallography

The mineralogy, lattice parameters, and crystallite size were determined by glancing angle X-ray diffraction (GAXRD; Philips PANalytical Diffractometer, CuK α , 45 kV and 40 mA, incident angle 1°, step size 0.0262° 2 θ , scanning rate 0.01° 2 θ sec⁻¹). The lattice parameters and unit cell volume were determined by Rietveld refinement analysis²⁷. The crystallite size was calculated using the Scherrer equation, which is based on the full width at half maximum (FWHM) of the GAXRD peaks²⁸. These data were calculated on the basis of both the main (101) peak and seven principal (*hkl*) peaks.

The mineralogy was confirmed by laser Raman microspectroscopy (Raman; Renishaw inVia Raman Microscope, argon ion laser, 514 nm (green laser), 25 mW, 50X, beam diameter 1.5 μ m, exposure time 30 s).

Morphology

The RMS and Ra roughnesses were assessed by atomic force microscopy (AFM; Bruker Dimension Icon SPM, tapping mode, nominal tip radius 7 nm). The mean grain size was examined by both AFM and transmission electron microscopy (TEM; Tecnai G2 20, 200 kV), processing data for ~150 grains for each thin film using *Image J*. Samples for the determination of film thickness by TEM were prepared by focused ion beam milling (FIB; FEI Nova 200 dual beam focused ion beam system, Ga source, fine-beam current 100 pA) to extract a thin cross section of the near-surface zone from the specimen (15 μ m x 15 μ m.). A thin layer of Pt was deposited prior to the FIB lift-out procedure in order to protect the surface.

Chemical Properties

The elemental distributions were examined by energy dispersive spectroscopy (EDS; Tecnai G2 20, 200 kV) using the same sample as examined by TEM. The surface chemistry was determined by X-ray photoelectron spectroscopy (XPS; Thermo Scientific ESCALAB 250Xi, 15.2 kV, 10.8 mA, spot size 500 μ m).

Optical Properties

The optical absorption and transmission were determined by ultraviolet-visible spectrophotometry (UV-Vis; PerkinElmer Lambda 35 UV-Visible spectrometer, dual beam). The optical indirect and direct E_g values were determined from the absorption data using the Tauc method²⁹, which involves determining the intercept of the linear section of the relevant curve with the abscissa.

Semiconducting Properties

The valence band position maxima also were determined by X-ray photoelectron spectroscopy (XPS; Thermo Scientific ESCALAB 250Xi, 15.2 kV, 10.8 mA, spot size 500 μm) by extrapolation of the XPS valence band data to nil intensity^{30,31}.

The Fermi energy was determined by amplitude-modulated Kelvin probe force microscopy (AM-KPFM; Bruker Dimension ICON SPM with a Nanoscope V controller). A platinum-iridium-coated AFM tip (Bruker, SCM-PIT-V2) was used to scan the surface. For calibration, before and after measuring the specimen, the work function change of the AFM tip was measured against that of a freshly cleaved and highly oriented pyrolytic graphite (HOPG) sample, where the work function (φ) of the HOPG is 4.6 eV versus vacuum ($\Delta V = (\varphi_{HOPG} - \varphi_{tip})/e$), where e is the electron charge³². For measurement, the lift height was fixed at 100 nm for all specimens in order to avoid influence from surface topography. The scan area was 5 μm x 5 μm and the scan rate was 0.6 Hz. The resolution of the image was set to 256 samples/line. The drive2 amplitude of the a.c. bias applied to the tip during the lift pass was set at 500 mV with a 170° phase angle.

2.4.3 Photocatalytic Performance

The photocatalytic performance was determined by photodegradation of standard dye under UV light. The aqueous dye solution (10^{-5} M) initially was adsorbed on the film surface by soaking each sample in 13 mL of the solution for 1 h in an opaque enclosure, after which the sample was removed and placed in 13 mL of fresh solution (both in 50 mL Pyrex beakers). All of the samples were exposed to ultraviolet radiation (3UV-38, UVP, 8 W, 365 nm) for 1, 3, 6, 9, 12, and 24 h. The lamp-meniscus and meniscus-film distances were 10 cm and 8 cm, respectively. Each photodegraded solution was analysed by UV-Vis using the maximal

absorption wavelength at 664 nm. The photodegradation efficiency and the photocatalytic reaction rate of the dye were calculated according to the Lambert-Beer law ³³.

3. RESULTS

Mineralogy and Crystallography

A range of annealing temperatures (350°, 450°, 550°, and 650°C) was investigated as shown in Figure 0, revealing that the lowest temperature was poorly recrystallised and the two highest temperatures were subject to latticed destabilisation and structural degradation. Hence, the maximal crystallinity was observed the annealing temperature of 450°C, so this was selected as the basis for the present work.

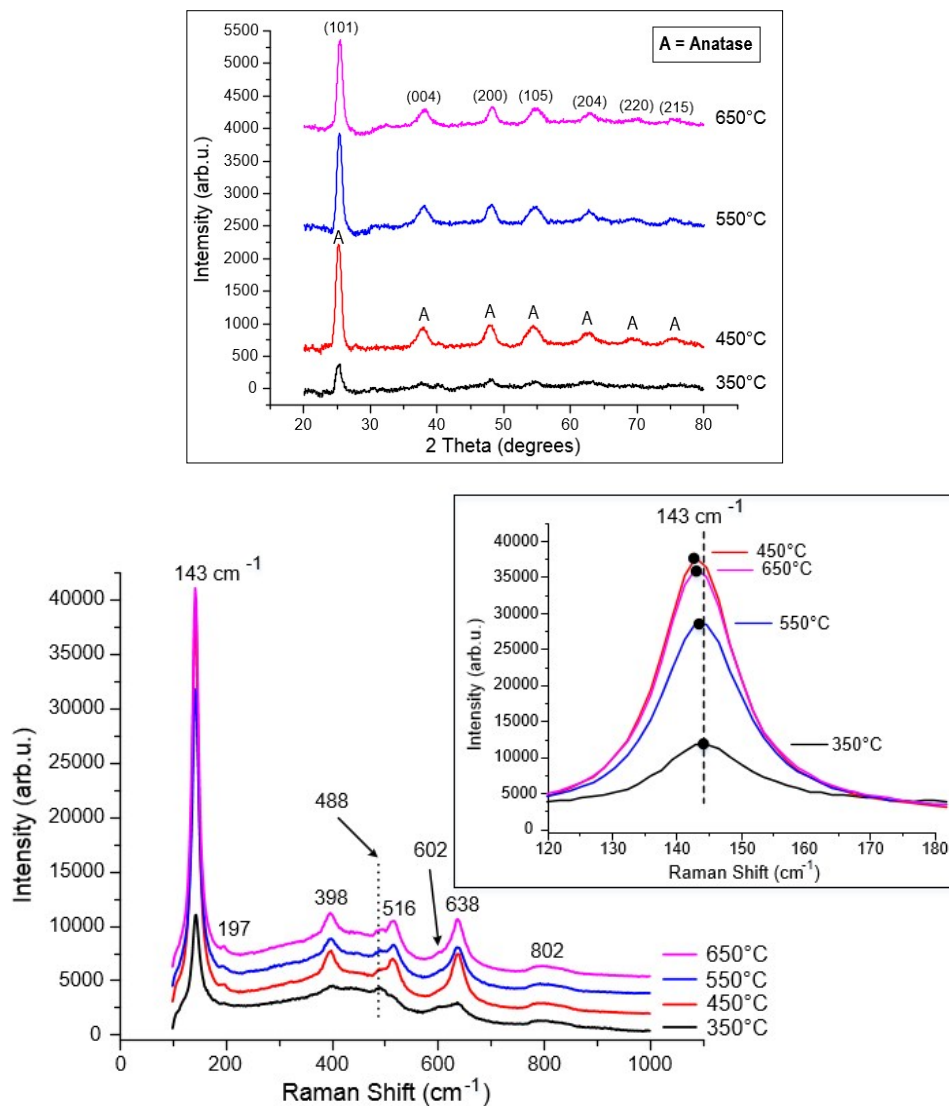


Figure 0. GAXRD patterns and laser Raman microspectra for undoped TiO₂ thin films annealed at 350°, 450°, 550° and 650°C for 2 h.

Figure I shows the GAXRD patterns of the undoped and doped thin films. These data indicate that anatase is the sole detectable phase and that low Ce-doping concentrations (≤ 0.09 mol%) appear to be associated with greater crystallinities but high Ce-doping concentrations (0.10-0.90 mol%) cause a gradual decrease in crystallinity.

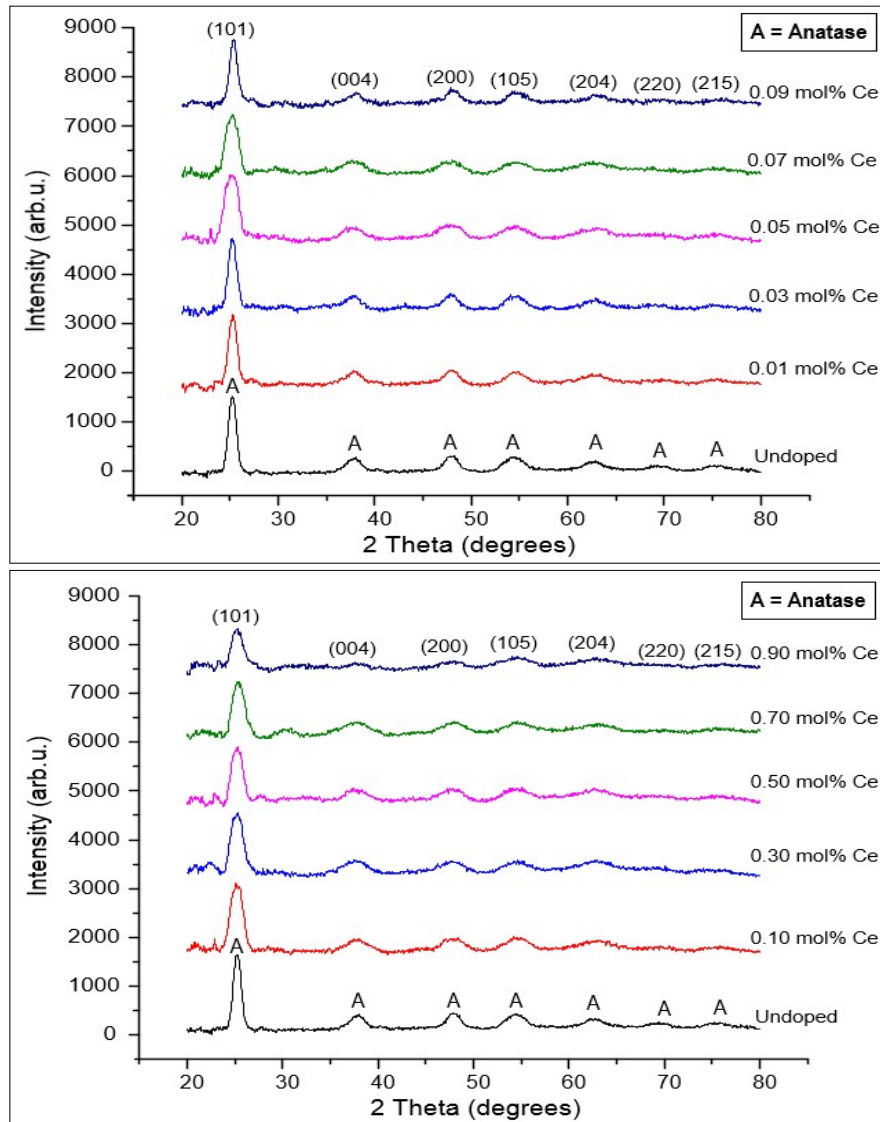


Figure I. GAXRD patterns of undoped and Ce-doped TiO_2 thin films with low (0.01-0.09 mol%) and high (0.10-0.90 mol%) Ce-doping concentrations, annealed at 450°C for 2 h.

Figure II shows the corresponding Raman patterns, which confirm the formation of anatase only and give greater clarity to the GAXRD data. That is, all levels of doping decrease the crystallinity relative to the undoped thin film. However, the low Ce-doping concentrations gradually increase the crystallinity while the high Ce-doping concentrations decrease it more abruptly. The peaks at 490 cm^{-1} and 605 cm^{-1} derive from the fused SiO_2 substrate.

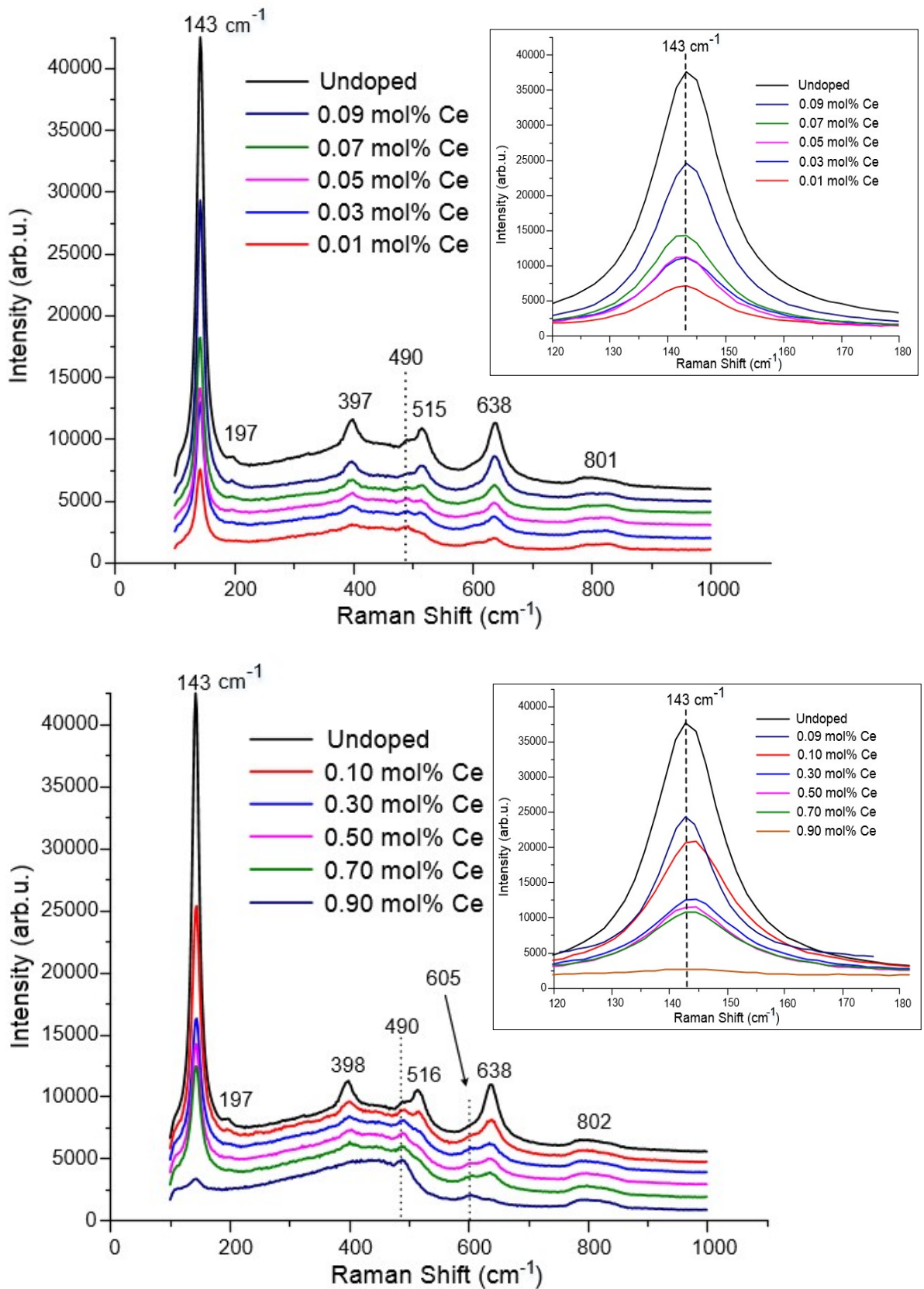
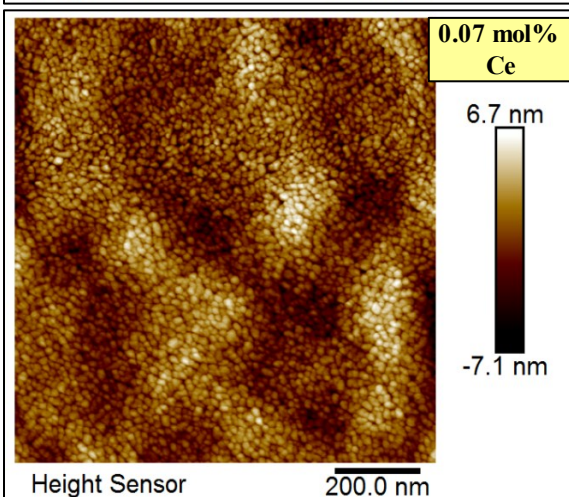
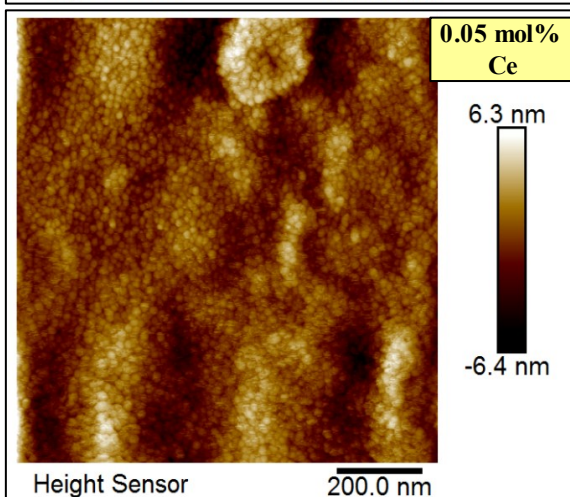
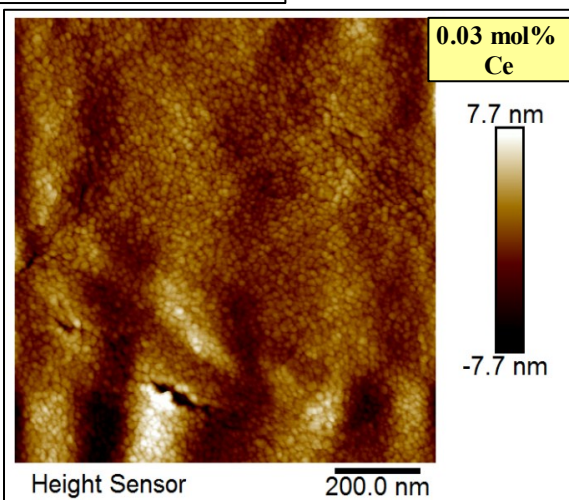
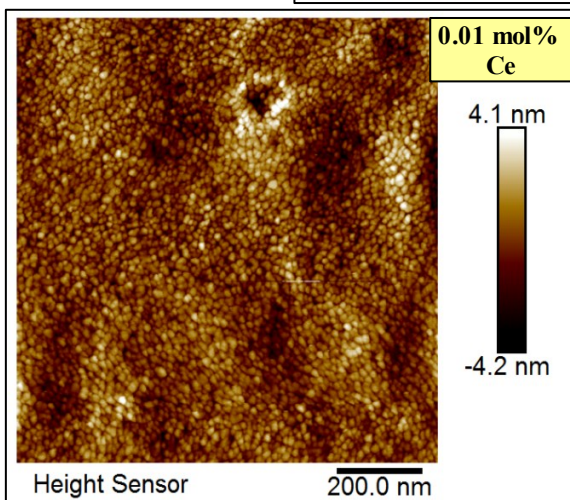
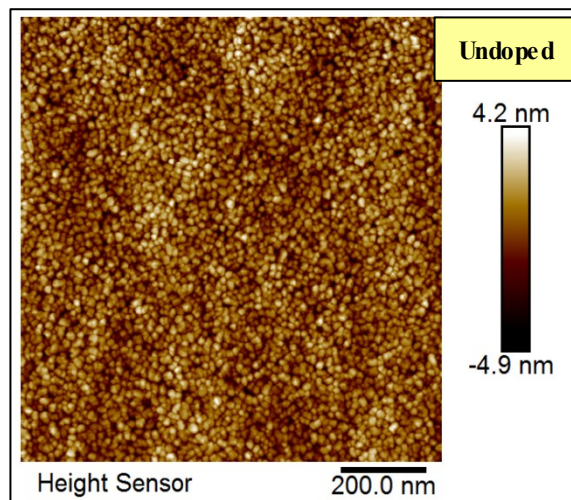


Figure II. Laser Raman microspectra for undoped and Ce-doped TiO_2 thin films with low (0.01-0.09 mol%) and high (0.10-0.90 mol%) Ce-doping concentrations, annealed at 450°C for 2 h; insert shows enlargement of 143 cm^{-1} main peak.

Morphology

Figure III shows the AFM data for the undoped and doped thin films in terms of the areal perspective (left) and depth scale (right); the associated data are tabulated in Table II. These data indicate that the low Ce-doping concentrations gradually increase the grain size but, following an abrupt decrease between 0.09 and 0.10 mol%, it decreases slightly. The roughness data are not as consistent, showing that doping initially causes a significant increase in grain size, with a gradual decrease for low Ce-doping concentrations. Following an abrupt decrease between 0.09 and 0.10 mol%, there is a gradual decrease for high Ce-doping concentrations. These data are contrary to expectation in that grain size decreases would be expected to result in roughness decreases; the converse is the case for the low Ce-doping concentrations. This is attributed to the increasing areal density of the grains with increasing Ce-doping concentration and the associated decreasing depth of the grain boundary groove, which is what the roughness reflects.



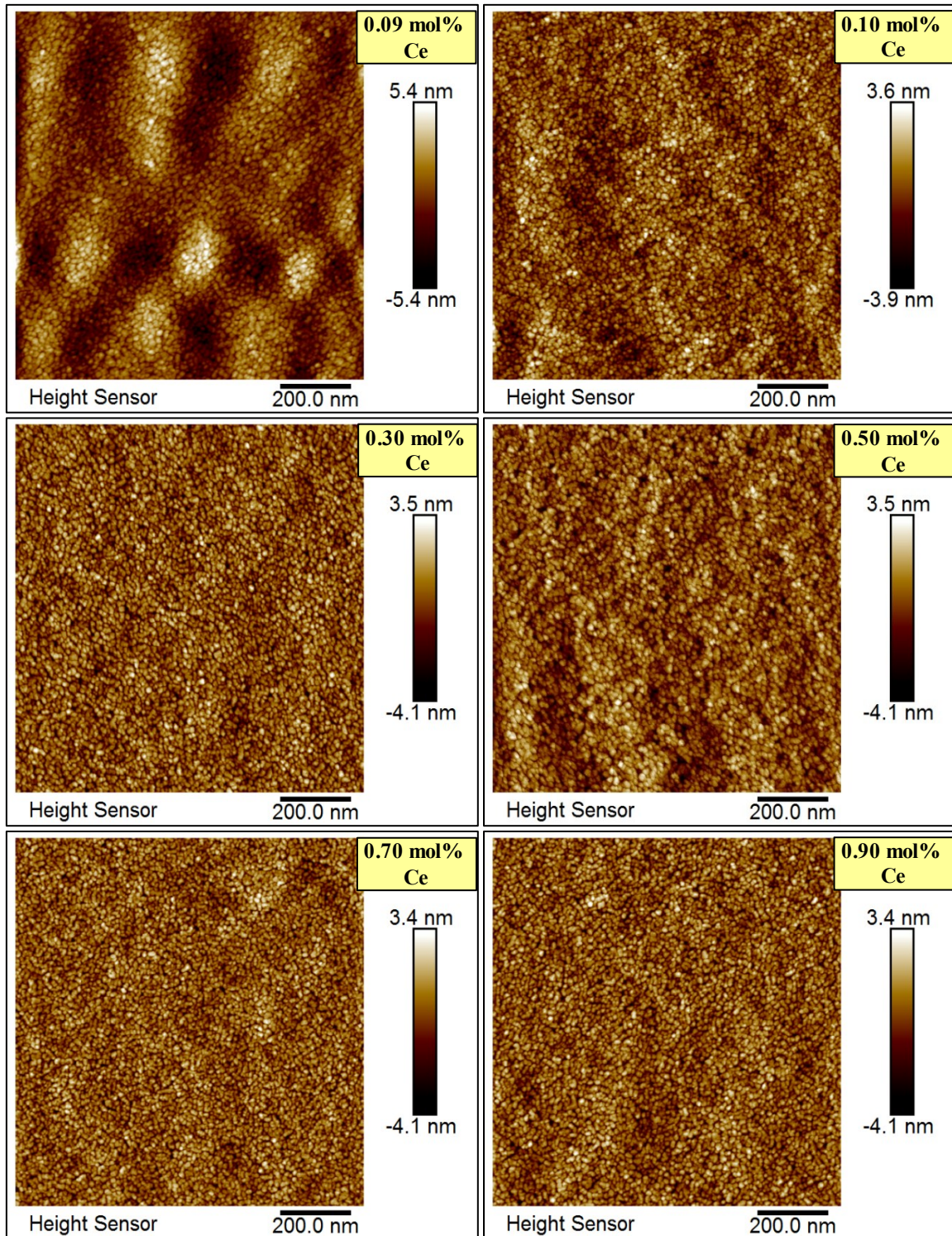
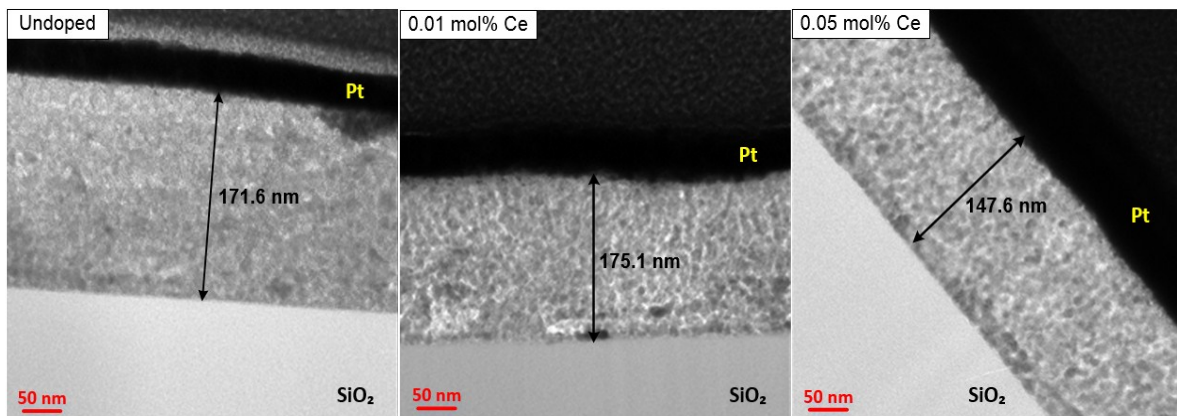


Figure III. AFM micrographs of undoped and Ce-doped TiO₂ thin films with low (0.01-0.09 mol%) and high (0.10-0.90 mol%) Ce-doping concentrations, annealed at 450°C for 2 h.

Table II. AFM and TEM data for undoped and Ce-doped TiO₂ thin films with low (0.01-0.09 mol%) and high (0.10-0.90 mol%) Ce-doping concentrations, annealed at 450°C for 2 h.

Sample (mol% Ce)	AFM			TEM	
	Mean Grain Size & Standard Deviation (nm)	RMS Roughness (nm)	Ra Roughness (nm)	Mean Grain Size & Standard Deviation (nm)	Mean Film Thickness (nm)
Undoped	7.5 ± 1.4	1.30	1.03	5.7 ± 1.7	171.6
0.01	8.0 ± 1.6	1.15	0.90	7.6 ± 1.6	175.1
0.03	8.7 ± 1.8	1.93	1.46	6.2 ± 1.1	253.7
0.05	9.0 ± 1.9	2.49	1.98	6.0 ± 1.2	147.6
0.07	9.2 ± 1.7	2.27	1.84	6.3 ± 1.1	227.3
0.09	9.5 ± 2.0	1.94	1.54	6.8 ± 1.5	241.1
0.10	7.6 ± 1.5	1.07	0.85	6.2 ± 1.1	192.1
0.30	7.5 ± 1.4	1.10	0.87	6.1 ± 1.1	234.7
0.50	7.4 ± 1.5	1.07	0.84	5.6 ± 1.3	170.0
0.70	7.1 ± 1.2	1.05	0.83	5.2 ± 1.3	217.5
0.90	6.7 ± 1.2	1.10	0.87	5.0 ± 1.3	199.5

Figure IV shows TEM cross sections of the thin films, indicating the film thicknesses and suggesting the grain sizes and dispositions; the associated data are tabulated in Table II. The film thicknesses were variable, with an average and standard deviation of 202 ± 34 nm; the range was $\sim 150 - 250$ nm. These variations are a reflection of the uneven profile of the unpolished fused SiO₂ substrates, which have an R_a roughness of 456 nm³⁴.



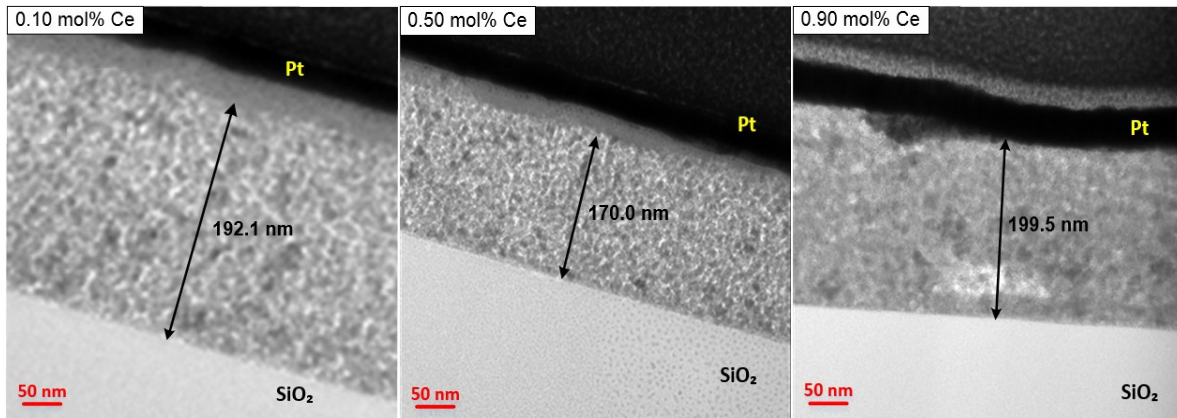


Figure IV. TEM micrographs of undoped and Ce-doped TiO_2 thin films with low (0.01-0.09 mol%) and high (0.10-0.90 mol%) Ce-doping concentrations, annealed at 450°C for 2 h.

Chemical Properties

The EDS data for the thin film with 0.10 mol% Ce are shown in Figure V. The line scan in Figure V(a) reveals that Ce is present as is Si. Although it normally would be considered that dissolved Si could affect the defect equilibria, this is not the case because it is known that Si is present only on the grain boundaries^{34, 35}, so the potential effect on photocatalysis would be limited to blockage of the surface-active sites. This conclusion is supported by the observation that the Si concentration does not exhibit a typical lattice diffusion profile^{36, 37}. Instead, it becomes constant, which is consistent with saturation of the grain boundary surfaces by adsorbed Si. Likewise, while it is possible that Ce is present only on the grain boundaries, subsequent GAXRD data confirm that Ce is dissolved in the anatase lattice. The elemental mapping in Figure V(b) shows homogeneous elemental distributions and essentially supports the line scan. Although the FIB sectioning could allow differentiation of the Si (grain circumference) and Ce (grain volume) distributions, the sensitivity of the EDS technique is insufficient for this to be done. However, the appearance of similar Si and Ce distributions in the elemental mapping supports the conclusion of the two respective diffusion mechanisms because the rapid Si grain boundary diffusion resulted in a higher but localised Si distribution and the slower Ce lattice diffusion resulted in a lower but homogeneous Ce distribution.

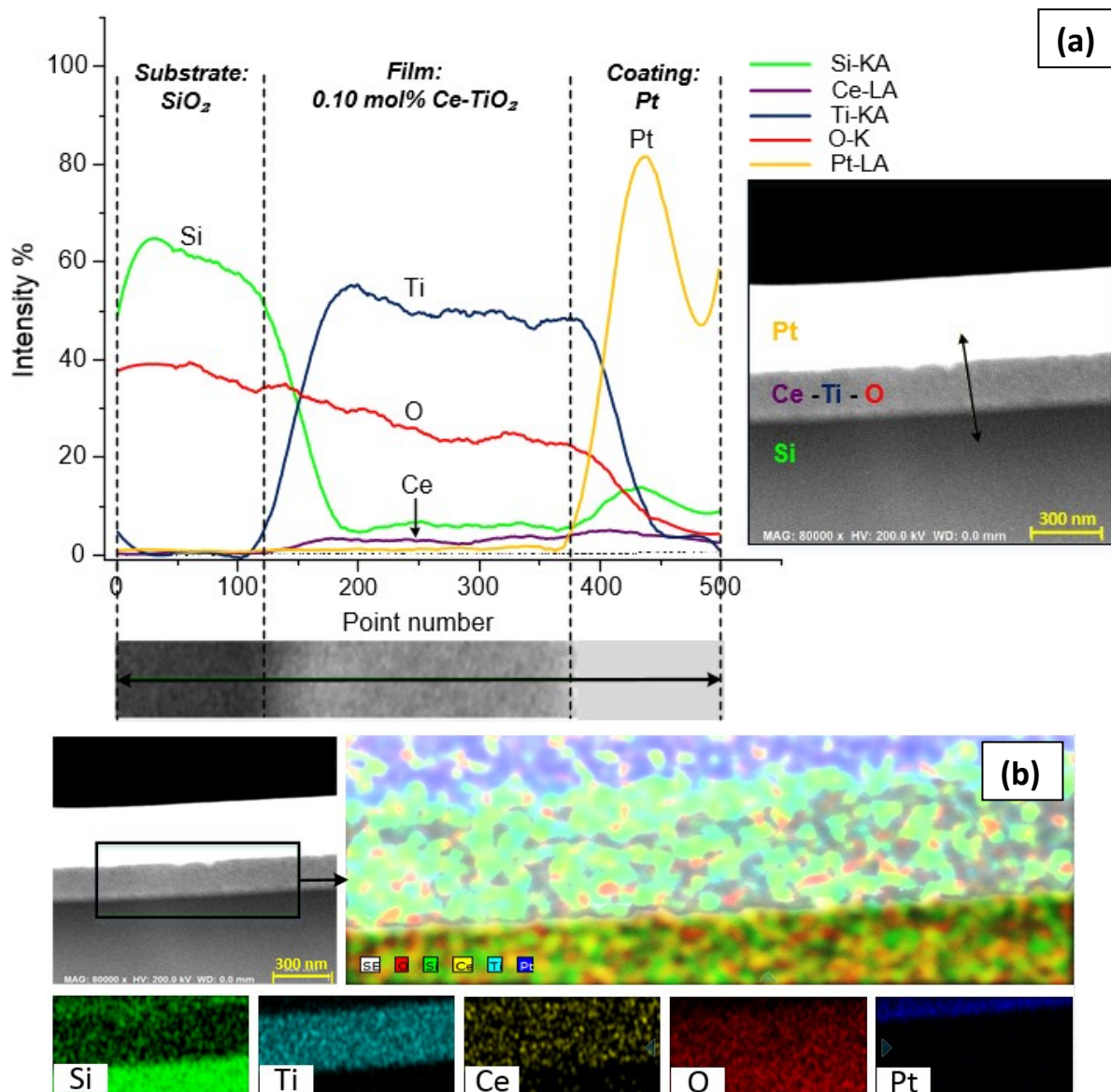
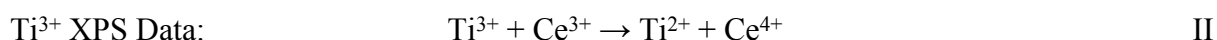
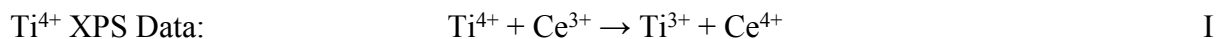


Figure V. (a) EDS line scan and (b) elemental mapping of 0.10 mol% Ce-doped TiO₂ thin film.

The XPS survey scans, which are not given, show that Ce-doping decreases the peak intensities for Ti from ~1 million counts (undoped) and ~900,000 counts (0.01 mol%) to ~480,000 counts (0.90 mol%). These large differences result from the greater sensitivity of the XPS technique³⁸ to Ce relative to Ti. Figure VI shows the Ti 2p overlapping XPS data for Ti^{4+/3+} and Figure VII shows the O 1s XPS data for Ti⁴⁺-O and Ti³⁺-O (which dominate the overlapping Ce⁴⁺-O and Ce³⁺-O data), both of which are intrinsic to TiO_{2-x}³⁵. All of the data indicate that, with increasing Ce doping concentration, relative to undoped TiO_{2-x}, both Ti valences decrease with Ce-doping up to 0.05 mol%, they increase and maximize at 0.09 mol% to a valence slightly less than that of the undoped TiO_{2-x}, and they decrease to

approximately constant valences for the higher Ce-doping concentrations. These data for the decreasing Ti valences at all Ce doping concentrations except 0.07 and 0.09 mol% Ce can be explained by IVCT according to the following indicative reactions:



If IVCT is the driving force for these Ti valence decreases (although Equation II is thermodynamically unlikely³⁹), then these data suggest that electron cloud proximity for charge transfer between Ti and Ce increases relative to undoped TiO_{2-x} over the ranges 0.00 – 0.05 mol% Ce and 0.09 – 0.90 mol% Ce in response to the Ti defect structure and the Ce solubility mechanism. Consequently, other Ti defect structures and/or solubility mechanisms reduce the electron cloud proximities over the range 0.05 – 0.09 mol% Ce.

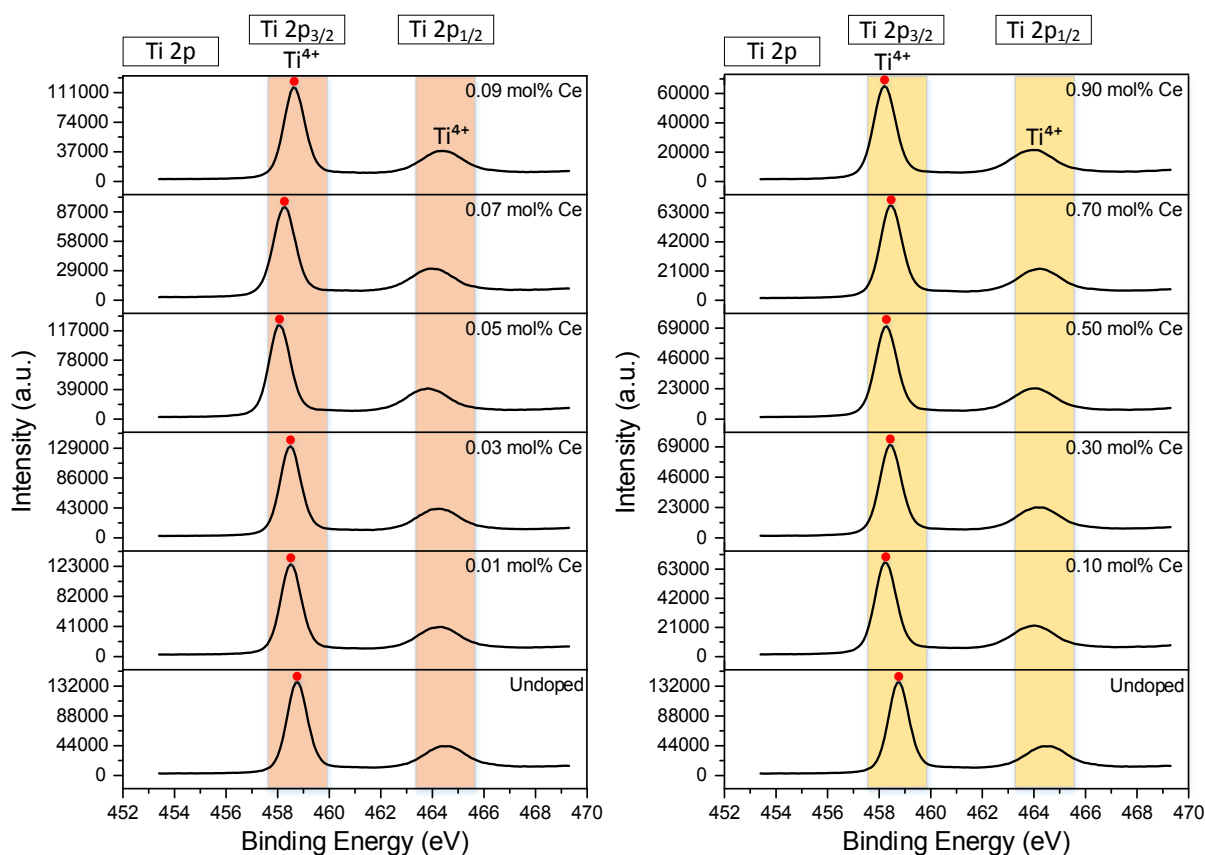


Figure VI. Ti 2p XPS spectra for Ti^{4+} of undoped and Ce-doped TiO_2 thin films with low (0.01-0.09 mol%) and high (0.10-0.90 mol%) Ce-doping concentrations, annealed at 450°C for 2 h (shaded regions = ranges of reported Ti binding energies).

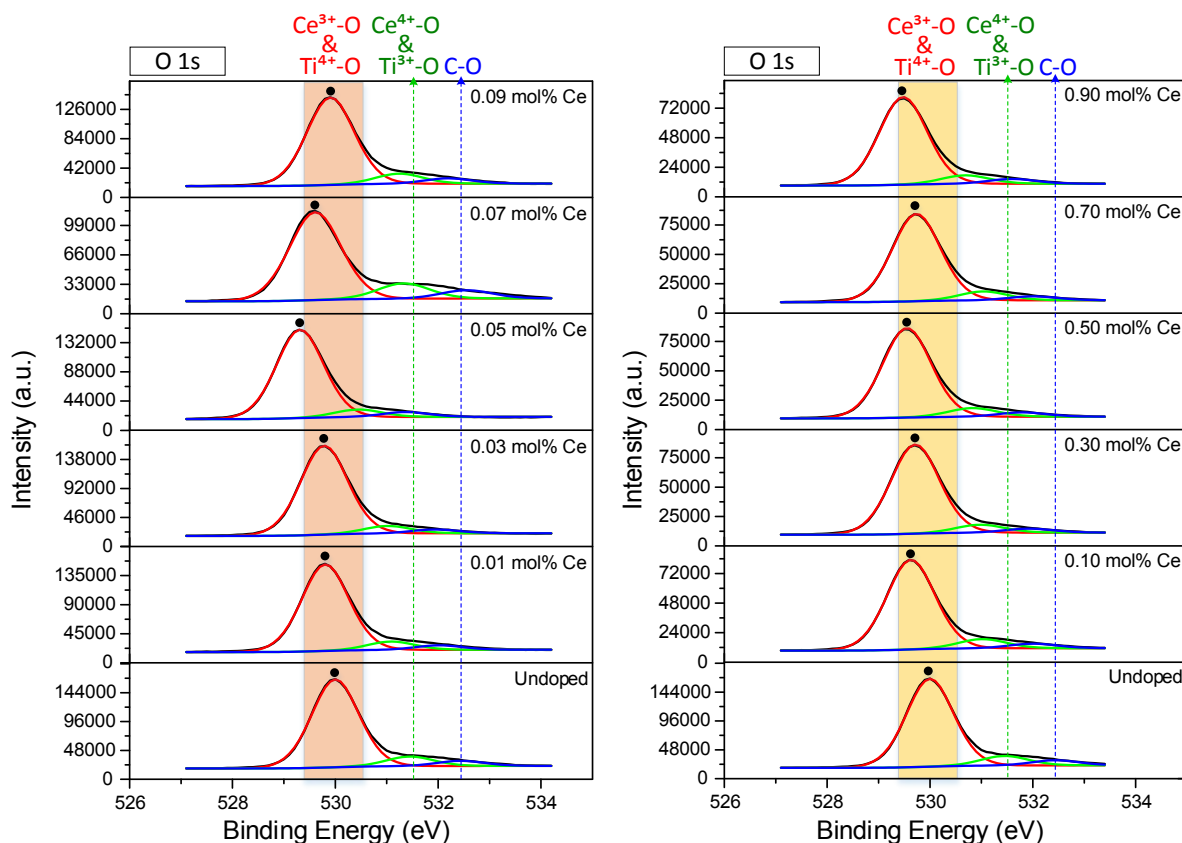


Figure VII. O 1s XPS spectra for $\text{Ti}^{4+}\text{-O}$, $\text{Ti}^{3+}\text{-O}$, $\text{Ce}^{4+}\text{-O}$, and $\text{Ce}^{3+}\text{-O}$ of undoped and Ce-doped TiO_2 thin films with low (0.01-0.09 mol%) and high (0.10-0.90 mol%) Ce-doping concentrations, annealed at 450°C for 2 h (shaded regions = ranges of reported Ti binding energies).

Figure VIII shows the Ce 3d XPS data for Ce^{4+} and Ce^{3+} , both of which are intrinsic to CeO_2 ⁴⁰, revealing that the majority valence is Ce^{3+} . This is unexpected since neither thermodynamics according to the stability diagram¹³ nor IVCT according to Equations I and II favours Ce^{4+} as a product of $\text{Ce}^{3+} \rightarrow \text{Ce}^{4+}$ oxidation during annealing in air. This is a critical observation because the increasing concentration of the precursor valence of Ce^{3+} thus demonstrates that Ce^{3+} dissolves directly in the lattice. However, the role of IVCT in generating the non-equilibrium valence Ti^{3+} from a Ti^{4+} precursor⁴¹ is confirmed by the overall trends (0.00-0.05 and 0.09-0.90 mol% Ce). Again, this is contrary to thermodynamics according to the stability diagram⁴².

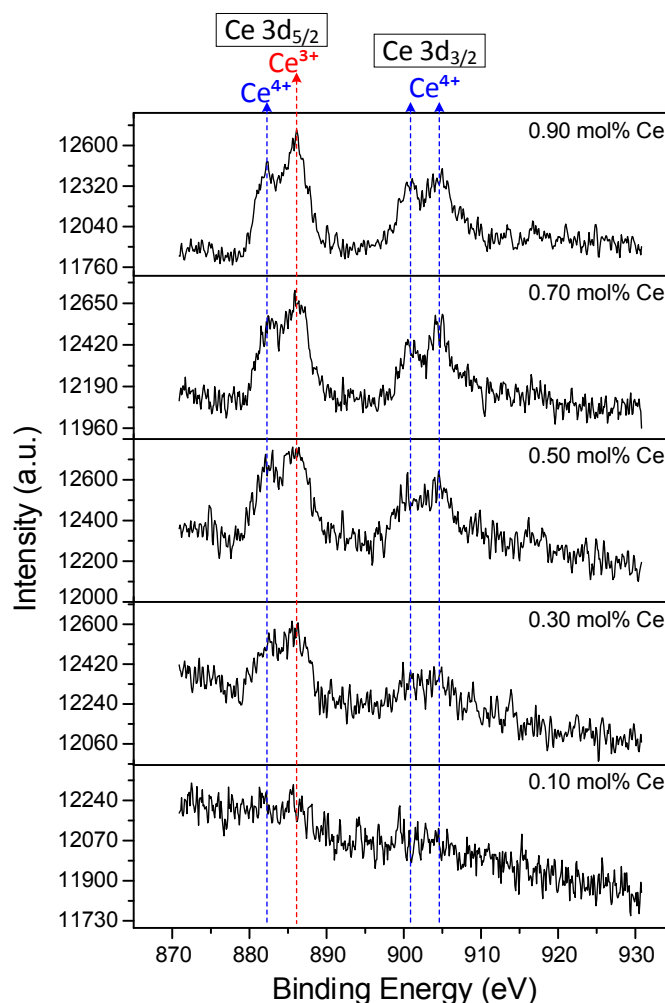


Figure VIII. Ce 3d XPS spectra for Ce⁴⁺ and Ce³⁺ of undoped and Ce-doped TiO₂ thin films with low (0.01-0.09 mol%) and high (0.10-0.90 mol%) Ce-doping concentrations, annealed at 450°C for 2 h.

Tables III⁴³ and IV (compensated) tabulate the graphical data in Figures VI-VIII as well as the oxygen vacancy concentrations ($[V_{O}^{\bullet\bullet}]$) calculated in principle from the Ti³⁺ concentrations ($[Ti^{3+}]$). While the presence of Ti³⁺ can derive from both ionic charge compensation (Equation 1, in the main manuscript) and IVCT (Equation 2, in the main manuscript), the presence of oxygen vacancies can derive only from ionic charge compensation (Equation 1, in the main manuscript). Since these data values, which show a maximum at 0.09 mol% Ce, are irregular, it is not clear if the governing mechanism of charge compensation occurs through oxygen vacancy formation, which is the generally held perspective^{35, 40, 42}. However, the trend variation centred at 0.09 mol% Ce suggests that there are at least two competing mechanisms. Since it is known that oxygen vacancy formation (substitutional solid solubility; Equations 8-11) and cation vacancy formation (interstitial solid solubility;

Equations 16-19) result in lattice expansion ^{44, 45} and contraction ⁴⁶⁻⁵⁰, respectively, then the charge compensation mechanism could be considered by contrasting potential defect equilibria with the lattice volume. This has been discussed more fully in Mechanism chapter (in the main manuscript).

Table III. XPS raw data for surface atomic concentrations for undoped and Ce-doped TiO₂ thin films with low (0.01-0.09 mol%) and high (0.10-0.90 mol%) Ce-doping concentrations, annealed at 450°C for 2 h.*

Sample (mol% Ce)	Surface Atomic Concentration (at%)										
	Ti ^{4+/3+} (2p) ^a	Ti ⁴⁺ -O (1s) ^{a,b}	Ti ³⁺ -O (1s) ^{a,b}	V _{Oc} ^{••}	Ti ⁴⁺		Ti ³⁺		Ti ³⁺ /Ti ⁴⁺ Peak Ratio ^a	Ce ^{4+/3+} (3d) ^a	Ce ⁴⁺ /Ce ³⁺ Peak Ratio ^a
					Calc. ^d	%	Calc. ^e	%			
Undoped	35.57	58.21	6.22	3.11	32.15	90.38	3.42	9.62	0.106	0.00	--
0.01	33.57	60.55	5.88	2.94	30.60	91.15	2.97	8.85	0.097	0.00	--
0.03	33.71	61.14	5.15	2.57	31.09	92.22	2.62	7.78	0.084	0.00	--
0.05	33.94	60.88	5.18	2.59	31.28	92.16	2.66	7.84	0.085	0.00	--
0.07	32.49	62.14	5.37	2.68	29.91	92.05	2.58	7.95	0.086	0.00	--
0.09	32.96	60.05	6.94	3.47	29.53	89.59	3.43	10.41	0.116	0.05	0.76
0.10	31.96	61.58	6.37	3.18	28.97	90.64	2.99	9.36	0.103	0.09	0.77
0.30	32.23	62.03	5.59	2.79	29.57	91.74	2.66	8.26	0.089	0.15	0.88
0.50	31.93	61.81	6.03	3.01	29.09	91.10	2.84	8.90	0.097	0.23	0.86
0.70	31.83	61.62	6.29	3.14	28.88	90.73	2.95	9.27	0.102	0.26	0.78
0.90	32.11	61.54	6.01	3.00	29.25	91.09	2.86	8.91	0.097	0.34	0.75

* The peak overlaps in Figure VII, which show Ce³⁺/Ti⁴⁺ and Ce⁴⁺/Ti³⁺ coincidence, were resolved as follows:

^a From peak areas

^b Peak overlaps with Ce⁴⁺-O (1s) [528.70-529.60 eV] and with Ce³⁺-O (1s) [529.00-530.30 eV]

^c Calculated from ½(Ti³⁺-O)

^d Calculated (Calc.) from Ti⁴⁺-O/(Ti⁴⁺-O + Ti³⁺-O)

^e Calculated (Calc.) from Ti³⁺-O/(Ti⁴⁺-O + Ti³⁺-O)

Table IV. XPS compensated data for surface atomic concentrations for undoped and Ce-doped TiO₂ thin films with low (0.01-0.09 mol%) and high (0.10-0.90 mol%) Ce-doping concentrations, annealed at 450°C for 2 h.*

Sample (mol% Ce)	Surface Atomic Concentration (at%)										
	Ti ^{4+/3+} – Ce ^{4+/3+} (2p) ^a	Ti ⁴⁺ -O (1s) ^{a,b}	Ti ³⁺ -O (1s) ^{a,b}	V _{Oc} ^{••}	Ti ⁴⁺		Ti ³⁺		Ti ³⁺ /Ti ⁴⁺ Peak Ratio ^a	Ce ^{4+/3+} (3d) ^a	Ce ⁴⁺ /Ce ³⁺ Peak Ratio ^a
					Calc. ^d	%	Calc. ^e	%			
Undoped	35.57	58.21	6.22	3.11	32.15	90.38	3.42	9.61	0.106	0.00	--
0.01	33.57	60.55	5.88	2.94	30.60	91.15	2.97	8.84	0.097	0.00	--
0.03	33.71	61.14	5.15	2.57	31.09	92.22	2.62	7.77	0.084	0.00	--
0.05	33.94	60.88	5.18	2.59	31.28	92.16	2.66	7.83	0.085	0.00	--
0.07	32.49	62.14	5.37	2.68	29.91	92.05	2.58	7.94	0.086	0.00	--
0.09	32.91	60.05	6.94	3.47	29.47	89.54	3.43	10.45	0.116	0.05	0.76
0.10	31.87	61.58	6.37	3.18	28.88	90.61	2.98	9.38	0.103	0.09	0.77
0.30	32.08	62.03	5.59	2.79	29.42	91.70	2.65	8.29	0.089	0.15	0.88
0.50	31.70	61.81	6.03	3.01	28.87	91.07	2.82	8.92	0.097	0.23	0.86
0.70	31.57	61.62	6.29	3.14	28.64	90.71	2.92	9.28	0.102	0.26	0.78
0.90	31.77	61.54	6.01	3.00	28.93	91.06	2.83	8.93	0.097	0.34	0.75

* The peak overlaps in Figure VII, which show Ce³⁺/Ti⁴⁺ and Ce⁴⁺/Ti³⁺ coincidence, were resolved as follows:

- (1) Ce^{4+/3+} was subtracted from Ti^{4+/3+} (from Table III) to give Ti^{4+/3+} – Ce^{4+/3+}
- (2) The proportions of Ti⁴⁺-O and Ti³⁺-O were used to calculate the Ti³⁺/Ti⁴⁺ Peak Ratio
- (3) The Ti³⁺/Ti⁴⁺ Peak Ratio was normalised in order to calculate normalised fractions of Ti⁴⁺ (Calc.) and Ti³⁺ (Calc.)

^a From peak areas

^b Peak overlaps with Ce⁴⁺-O (1s) [528.70-529.60 eV] and with Ce³⁺-O (1s) [529.00-530.30 eV]

^c Calculated from ½(Ti³⁺-O)

^d Calculated (Calc.) from Ti⁴⁺-O/(Ti⁴⁺-O + Ti³⁺-O)

^e Calculated (Calc.) from Ti³⁺-O/(Ti⁴⁺-O + Ti³⁺-O)

Optical Properties

Figure IX shows the UV-Vis absorbance and transmittance spectra for the thin films. These data indicate that the films are relatively flat and nanostructurally homogeneous, as evidenced by the interference fringes. The optical direct and indirect band gaps (E_g) calculated by the Tauc method²⁹ are given in Table V and the graphs are shown in Figure X. These data indicate that initial doping raised both E_g values, they decreased to a minimum equivalent that of undoped TiO_2 at 0.09-0.10 mol%, and increased at higher Ce doping concentrations. Again, these data are indicative of the contributions from different mechanisms.

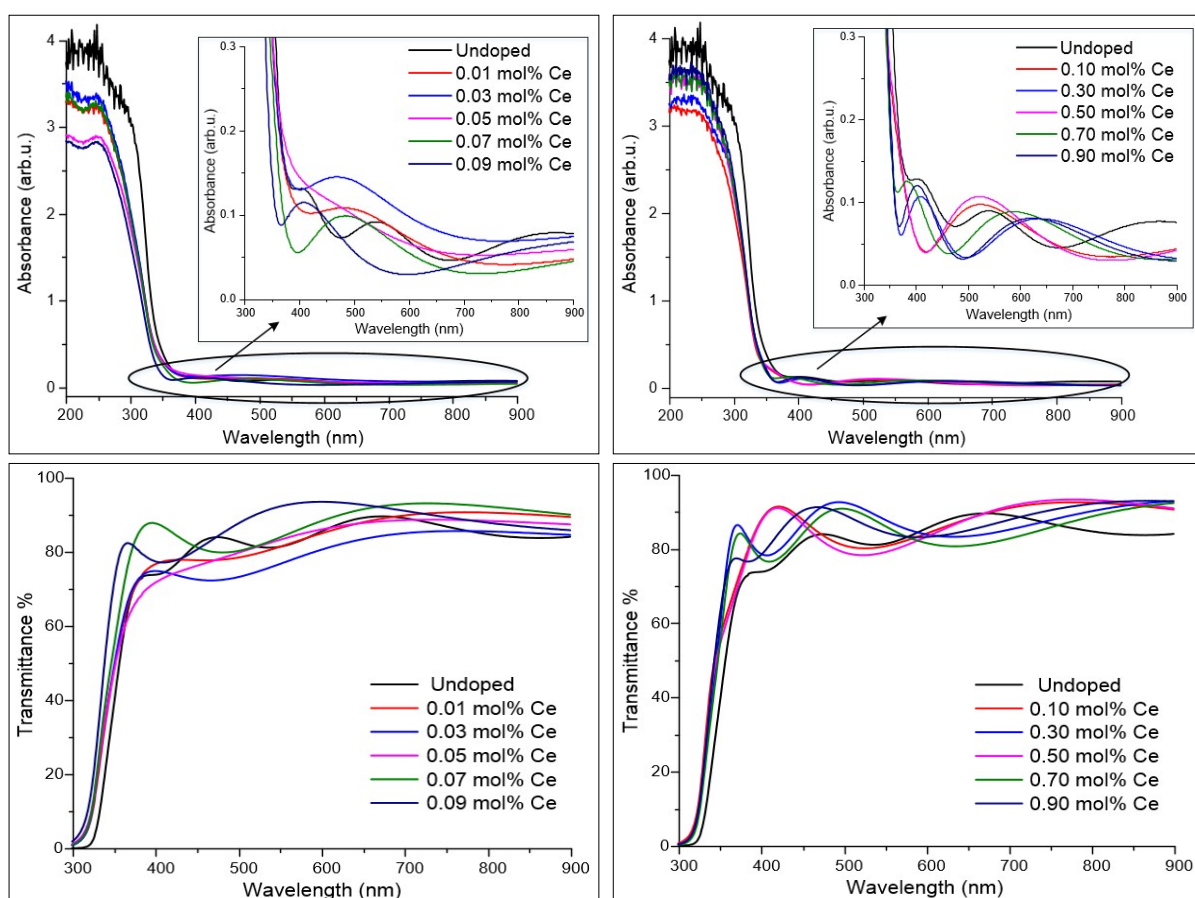


Figure IX. UV-Vis Absorbance and transmittance spectra for undoped and Ce-doped TiO_2 thin films with low (0.01-0.09 mol%) and high (0.10-0.90 mol%) Ce-doping concentrations, annealed at 450°C for 2 h.

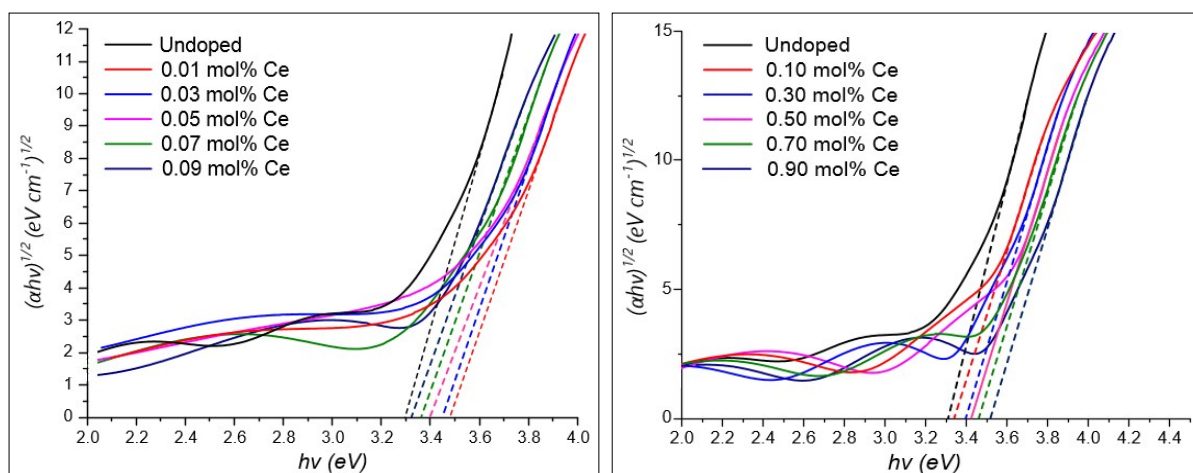


Figure X Indirect band gap graphs of undoped and Ce-doped TiO₂ thin films with low (0.01-0.09 mol%) and high (0.10-0.90 mol% Ce-doping concentrations, annealed at 450°C for 2 h.

Table V. Calculated band gaps for undoped and Ce-doped TiO₂ thin films with low (0.01-0.09 mol%) and high (0.10-0.90 mol% Ce-doping concentrations, annealed at 450°C for 2 h.

Sample (mol% Ce)	UV-Vis	
	Optical Direct Band Gap (eV)	Optical Indirect Band Gap (eV)
Undoped	3.70	3.30
0.01	3.78	3.49
0.03	3.77	3.45
0.05	3.75	3.40
0.07	3.73	3.38
0.09	3.71	3.32
0.10	3.72	3.31
0.30	3.74	3.40
0.50	3.76	3.42
0.70	3.78	3.47
0.90	3.80	3.51

Semiconducting Properties

Figure XI shows the XPS valence spectra for the thin films. The data indicate that the VBM values and the deviation from the E_f value initially increase and then decrease to 0.10 mol%, after which they increase. Again, these data can be attributed to the effects of different mechanisms.

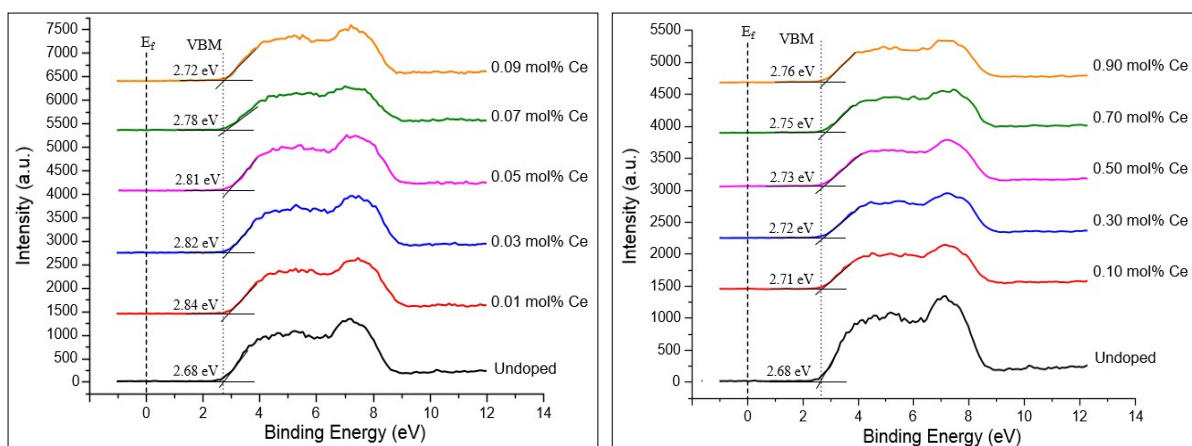


Figure XI. XPS valence spectra for undoped and Ce-doped TiO₂ thin films with low (0.01-0.09 mol%) and high (0.10-0.90 mol%) Ce-doping concentrations, annealed at 450°C for 2 h.

The surface potential differences between sample and platinum tip for 0.10 mol% Ce-doped sample is shown in Figure XII. The equation $\Delta V = (\varphi_{tip} - \varphi_{sample})/e$ yields φ_{sample} and E_f versus NHE.

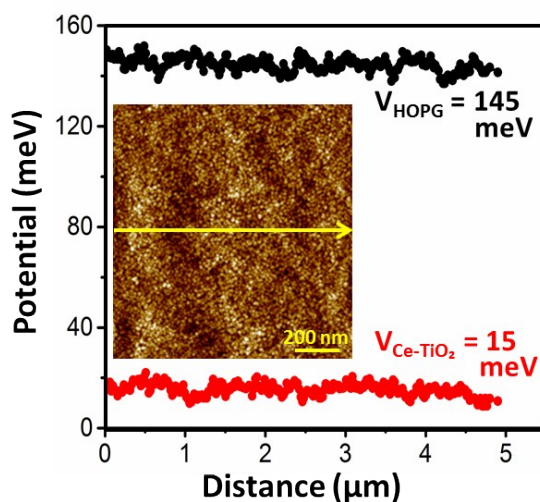


Figure XII. Average contact potential differences as line scan profiles for 0.10 mol% Ce-doped anatase.

Photocatalytic Performance

The photocatalytic performances of the thin films are shown in Figure XIII. These data show that low Ce-doping concentrations decrease the performance up to 0.09 mol% but that higher Ce-doping concentrations reverse the trend but without significant levels of differentiation

between doping concentrations. Yet again, it is clear that there are different mechanisms responsible for these data.

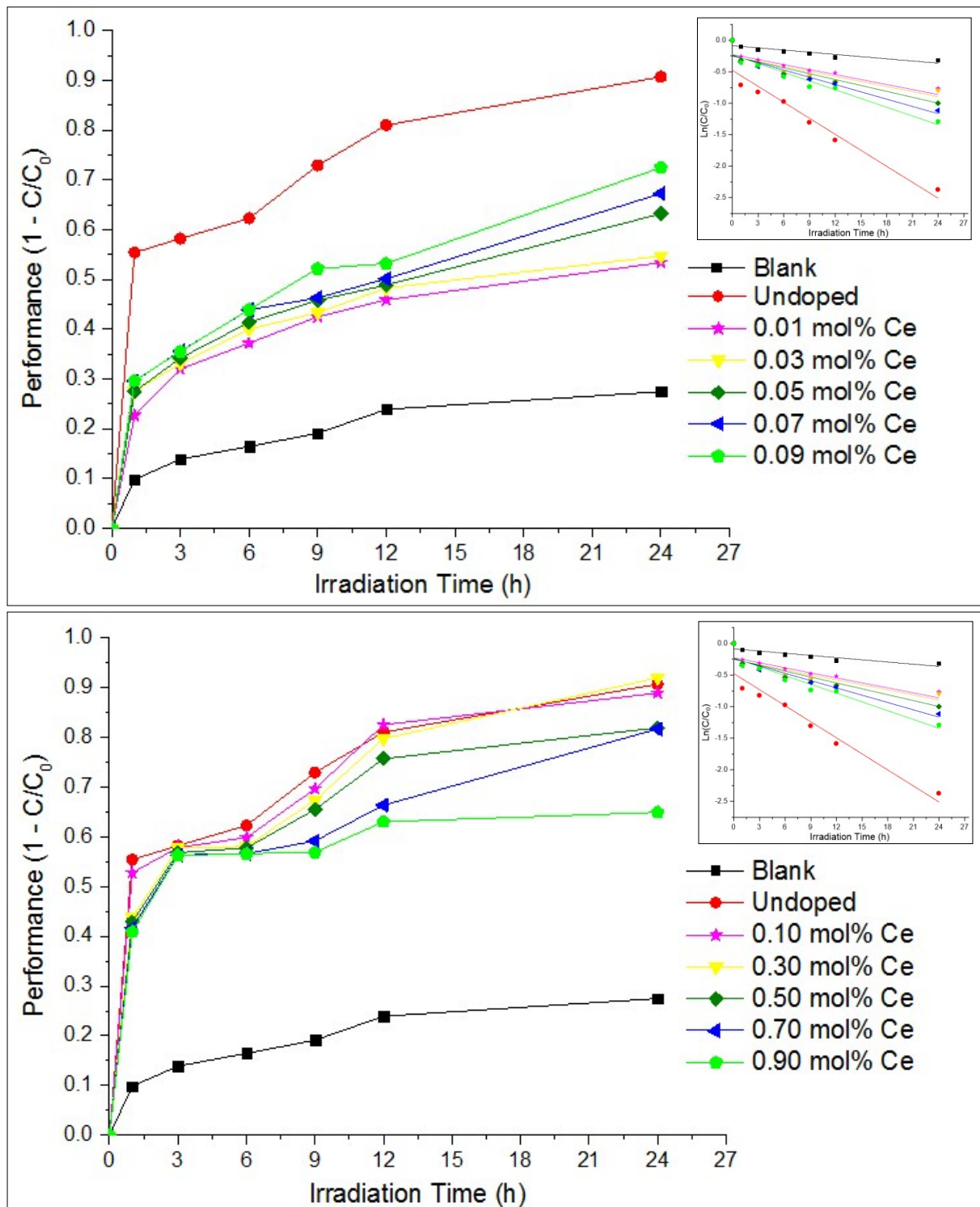


Figure XIII. UV-light photodegradation of MB solution and linear plots of $\ln(C/C_0)$ at different irradiation times photocatalysed by undoped and Ce-doped TiO_2 thin films with low (0.01-0.09 mol%) and high (0.10-0.90 mol%) Ce-doping concentrations, annealed at 450°C for 2 h.

References

1. Marimuthu, T.; Anandhan, N.; Rajendran, S.; Mummoorthy, M.; Vidhya, M., Studies on Pure and Ce Doped TiO₂ Thin Films Prepared by Sol-Gel Technique. *International Journal of ChemTech Research* **2014**, *6*, 5309-5314.
2. Popa, M.; Indrea, E.; Pascuta, P.; Cosoveanu, V.; Popescu, I.C.; Danciu, V., Fe, Ce and Cu Influence on Morpho-Structural and Photocatalytic Properties of TiO₂ Aerogels. *Revue Roumaine de Chimie* **2010**, *55*, 369-375.
3. Li, G.; Zhang, D.; Jimmy, C.Y., Thermally Stable Ordered Mesoporous CeO₂/TiO₂ Visible-Light Photocatalysts. *Physical Chemistry Chemical Physics* **2009**, *11*, 3775-3782.
4. Wang, Y.; Wu, Y.; Yang, H.; Xue, X.; Liu, Z., Doping TiO₂ With Boron or/and Cerium Elements: Effects on Photocatalytic Antimicrobial Activity. *Vacuum* **2016**, *131*, 58-64.
5. Xue, W.; Zhang, G.; Xu, X.; Yang, X.; Liu, C.; Xu, Y., Preparation of Titania Nanotubes Doped With Cerium and Their Photocatalytic Activity for Glyphosate. *Chemical Engineering Journal* **2011**, *167*, 397-402.
6. Zhang, J.; Peng, W.; Chen, Z.; Chen, H.; Han, L., Effect of Cerium Doping in the TiO₂ Photoanode on the Electron Transport of Dye-Sensitized Solar Cells. *The Journal of Physical Chemistry C* **2012**, *116*, 19182-19190.
7. Sidheswaran, M.; Tavlarides, L.L., Characterization and Visible Light Photocatalytic Activity of Cerium-and Iron-Doped Titanium Dioxide Sol- Gel Materials. *Industrial & Engineering Chemistry Research* **2009**, *48*, 10292-10306.
8. Wang, C.; Ao, Y.; Wang, P.; Hou, J.; Qian, J.; Zhang, S., Preparation, Characterization, Photocatalytic Properties of Titania Hollow Sphere Doped with Cerium. *Journal of Hazardous Materials* **2010**, *178*, 517-521.
9. Hongfen, W.; Zhiqi, W.; Haixia, H., Preparation of Cerium-Doped TiO₂ Film on 304 Stainless Steel and its Bactericidal Effect in the Presence of Sulfate-Reducing Bacteria (SRB). *Materials Chemistry and Physics* **2010**, *124*, 791-794.
10. Mardare, D.; Tasca, M.; Delibas, M.; Rusu, G., On the Structural Properties and Optical Transmittance of TiO₂ RF Sputtered Thin Films. *Applied Surface Science* **2000**, *156*, 200-206.
11. Zhang, Y.; Yuwono, A.H.; Wang, J.; Li, J., Enhanced Photocatalysis by Doping Cerium into Mesoporous Titania Thin Films. *The Journal of Physical Chemistry C* **2009**, *113*, 21406-21412.
12. Fan, C.; Xue, P.; Sun, Y., Preparation of Nano-TiO₂ Doped with Cerium and its Photocatalytic Activity. *Journal of Rare Earths* **2006**, *24*, 309-313.
13. Chung, L.; Chen, W.F.; Koshy, P.; Sorrell, C.C., Effect of Ce-doping on the Photocatalytic Performance of TiO₂ Thin Films. *Materials Chemistry and Physics* **2017**, *197*, 236-239.
14. Yan, Q.Z.; Su, X.T.; Huang, Z.Y.; Ge, C.C., Sol-gel Auto-Igniting Synthesis and Structural Property of Cerium-Doped Titanium Dioxide Nanosized Powders. *Journal of the European Ceramic Society* **2006**, *26*, 915-921.
15. Magesh, G.; Viswanathan, B.; Viswanath, R.; Varadarajan, T., Photocatalytic Behavior of CeO₂-TiO₂ System for the Degradation of Methylene Blue. *Indian Journal of Chemistry* **2009**, *48*, 480-488.
16. Albuquerque, A.R.; Bruix, A.; Sambrano, J.R.; Illas, F., Theoretical Study of the Stoichiometric and Reduced Ce-Doped TiO₂ Anatase (001) Surfaces. *The Journal of Physical Chemistry C* **2015**, *119*, 4805-4816.
17. Amrhein, K.; Stephan, D., Principles and Test Methods for the Determination of the Activity of Photocatalytic Materials and Their Application to Modified Building Materials. *Photochemical & Photobiological Sciences* **2011**, *10*, 338-342.
18. Saksornchai, E.; Kavinchan, J.; Thongtem, S.; Thongtem, T., The Photocatalytic Application of Semiconductor Stibnite Nanostructure Synthesized via a Simple Microwave-Assisted Approach in Propylene Glycol for Degradation of Dye Pollutants and its Optical Property. *Nanoscale Research Letters* **2017**, *12*, 589-599.

19. Sun, S.; Yu, X.; Yang, Q.; Yang, Z.; Liang, S., Mesocrystals for Photocatalysis: a Comprehensive Review on Synthesis Engineering and Functional Modifications. *Nanoscale Advances* **2019**, *1*, 34-63.
20. Perdew, J. P.; Ruzsinszky, A.; Csonka, G.I.; Vydrov, O.A.; Scuseria, G.E.; Constantin, L.A.; Zhou, X.; Burke, K., Restoring the Density-Gradient Expansion for Exchange in Solids and Surfaces. *Physical Review Letters* **2008**, *100*, 136406.
21. Kresse, G.; Furthmüller, J., Efficient Iterative Schemes for ab Initio Total-Energy Calculations Using a Plane-Wave Basis Set. *Physical Review B* **1996**, *54*, 11169.
22. Dudarev, S.; Botton, G.; Savrasov, S.; Humphreys, C.; Sutton, A., Electron-Energy-Loss Spectra and the Structural Stability of Nickel Oxide: An LSDA+ U Study. *Physical Review B* **1998**, *57*, 1505.
23. Albuquerque, A.R.; Bruix, A.; Dos Santos, I.d. M.; Sambrano, J.R.; Illas, F., DFT Study on Ce-Doped Anatase TiO₂: Nature of Ce³⁺ and Ti³⁺ Centers Triggered by Oxygen Vacancy Formation. *The Journal of Physical Chemistry C* **2014**, *118*, (18), 9677-9689.
24. Blöchl, P.E., Projector Augmented-Wave Method. *Physical Review B* **1994**, *50*, 17953.
25. Monkhorst, H.J.; Pack, J.D., Special Points for Brillouin-Zone Integrations. *Physical Review B* **1976**, *13*, 5188.
26. Brothers, E.N.; Izmaylov, A.F.; Normand, J.O.; Barone, V.; Scuseria, G.E., Accurate Solid-State Band Gaps via Screened Hybrid Electronic Structure Calculations. *The Journal of Chemical Physics* **2008**, *129*, 10.1063-1.2955460
27. Thompson, P.; Cox, D.; Hastings, J., Rietveld Refinement of Debye–Scherrer Synchrotron X-Ray Data from Al₂O₃. *Journal of Applied Crystallography* **1987**, *20*, 79-83.
28. Holzwarth, U.; Gibson, N., The Scherrer Equation Versus the 'Debye-Scherrer Equation'. *Nature Nanotechnology* **2011**, *6*, 534.
29. Dolgonos, A.; Mason, T.O.; Poeppelmeier, K.R., Direct Optical Band Gap Measurement in Polycrystalline Semiconductors: A Critical Look at the Tauc Method. *Journal of Solid State Chemistry* **2016**, *240*, 43-48.
30. Wu, X.; Ng, Y.H.; Wang, L.; Du, Y.; Dou, S.X.; Amal, R.; Scott, J., Improving the Photo-Oxidative Capability of BiOBr via Crystal Facet Engineering. *Journal of Materials Chemistry A* **2017**, *5*, 8117-8124.
31. Datta, R.S.; Ou, J.Z.; Mohiuddin, M.; Carey, B.J.; Zhang, B.Y.; Khan, H.; Syed, N.; Zavabeti, A.; Haque, F.; Daeneke, T., Two Dimensional PbMoO₄: A Photocatalytic Material Derived from a Naturally Non-Layered Crystal. *Nano Energy* **2018**, *49*, 237-246.
32. Beerbom, M.; Lägél, B.; Cascio, A.; Doran, B.; Schlaf, R., Direct Comparison of Photoemission Spectroscopy and in Situ Kelvin Probe Work Function Measurements on Indium Tin Oxide Films. *Journal of Electron Spectroscopy and Related Phenomena* **2006**, *152*, 12-17.
33. Swinehart, D., The Beer-Lambert Law. *Journal of Chemical Education* **1962**, *39*, 333.
34. Kabir, I.; Sheppard, L.; Liu, R.; Yao, Y.; Zhu, Q.; Chen, W.F.; Koshy, P.; Sorrell, C., Contamination of TiO₂ Thin Films Spin Coated on Rutile and Fused Silica Substrates. *Surface and Coatings Technology* **2018**, *354*, 369-382.
35. Chen, W.F.; Koshy, P.; Sorrell, C.C., Effect of Intervalence Charge Transfer on Photocatalytic Performance of Cobalt-and Vanadium-Codoped TiO₂ Thin Films. *International Journal of Hydrogen Energy* **2015**, *40*, 16215-16229.
36. Kofstad, P., *Nonstoichiometry, Diffusion, and Electrical Conductivity in Binary Metal Oxides*. John Wiley & Sons, Inc: New York, 1972.
37. Kofstad, P., *High Temperature Oxidation of Metals*. J John Wiley & Sons, Inc., New York, 1966, pp 340.
38. Barth, C.; Laffon, C.; Olbrich, R.; Ranguis, A.; Parent, P.; Reichling, M., A Perfectly Stoichiometric and Flat CeO₂ (111) Surface on a Bulk-Like Ceria Film. *Scientific Reports* **2016**, *6*, Article 21165.
39. Ortiz, L. A.A Spectroscopic and Electrochemical Study of Chlorotitanates in Molten Salt Media. Ph.D. Thesis, Massachusetts Institute of Technology, Cambridge, Massachusetts, 2000.

40. Chen, W.F.; Mofarah, S.S.; Hanaor, D.A. H.; Koshy, P.; Chen, H.K.; Jiang, Y.; Sorrell, C.C., Enhancement of Ce/Cr Codopant Solubility and Chemical Homogeneity in TiO₂ Nanoparticles Through Sol–Gel Versus Pechini Syntheses. *Inorganic Chemistry* **2018**, *57*, 7279-7289.
41. Archaapinun, K.; Witit-Anun, N.; Visuttipitukul, P., Effect of Heat Treatment on Phase Transformation of TiO₂ and Its Reflectance Properties. *Journal of Metals, Materials and Minerals* **2013**, *23*, 43-49.
42. Chen, W.F.; Chen, H.; Koshy, P.; Nakaruk, A.; Sorrell, C.C., Effect of Doping on the Properties and Photocatalytic Performance of Titania Thin Films on Glass Substrates: Single-ion Doping with Cobalt or Molybdenum. *Materials Chemistry and Physics* **2018**, *205*, 334-346
43. Rawat, J.; Rana, S.; Sorensson, M.; Misra, R., Anti-Microbial Activity of Doped Anatase Titania Coated Nickel Ferrite Composite Nanoparticles. *Materials Science and Technology* **2007**, *23*, 97-102.
44. Santara, B.; Giri, P.; Imakita, K.; Fujii, M., Microscopic Origin of Lattice Contraction and Expansion in Undoped Rutile TiO₂ Nanostructures. *Journal of Physics D: Applied Physics* **2014**, *47*, 215302.
45. Aidhy, D.S.; Liu, B.; Zhang, Y.; Weber, W.J., Chemical Expansion Affected Oxygen Vacancy Stability in Different Oxide Structures from First Principles Calculations. *Computational Materials Science* **2015**, *99*, 298-305.
46. D'Angelo, A.M.; Chaffee, A.L., Correlations Between Oxygen Uptake and Vacancy Concentration in Pr-Doped CeO₂. *ACS Omega* **2017**, *2*, 2544-2551.
47. Tilley, R.J.D., *Defects in Solids*, John Wiley & Sons, Hoboken, NJ, 2008.
48. Inaba, H.; Tagawa, H., Ceria-Based Solid Electrolytes. *Solid State Ionics* **1996**, *83*, 1-16.
49. Kim, D.J., Lattice Parameters, Ionic Conductivities, and Solubility Limits in Fluorite-Structure MO₂ Oxide [M= Hf⁴⁺, Zr⁴⁺, Ce⁴⁺, Th⁴⁺, U⁴⁺] Solid Solutions. *Journal of the American Ceramic Society* **1989**, *72*, 1415-1421.
50. Grey, I. E.; Wilson, N.C., Titanium Vacancy Defects in Sol–Gel Prepared Anatase. *Journal of Solid State Chemistry* **2007**, *180*, 670-678.